3D reconstruction of SARS-CoV-2 infection in ferrets emphasizes focal infection pattern in the upper respiratory tract

Luca M. Zaeck[1], David Scheibner[1], Julia Sehl[2], Martin Müller[1], Donata Hoffmann[3], Martin Beer[3], Elsayed M. Abdelwhab[1], Thomas C. Mettenleiter[4], Angele Breithaupt[2], Stefan Finke[1,*]

[1]Institute of Molecular Virology and Cell Biology, Friedrich-Loeffler-Institut, Federal Research Institute for Animal Health, 17493 Greifswald, Isle of Riems, Germany

[2]Department of Experimental Animal Facilities and Biorisk Management, Friedrich-Loeffler-Institut, Federal Research Institute for Animal Health, 17493 Greifswald, Isle of Riems, Germany

[3]Institute of Diagnostic Virology, Friedrich-Loeffler-Institut, Federal Research Institute for Animal Health, 17493 Greifswald, Isle of Riems, Germany

[4]Friedrich-Loeffler-Institut, Federal Research Institute for Animal Health, 17493 Greifswald, Isle of Riems, Germany

Short title: 3D Analysis of SARS-CoV-2 Infection in Ferrets

word count (abstract): 150

word count (total): 7776; character count (total): 54162

page count (total): 22

*Corresponding author:

Stefan Finke; tel.: +49 38351 71283; e-mail address: stefan.finke@fli.de

Abstract

The visualization of viral pathogens in infected tissues is an invaluable tool to understand spatial virus distribution, localization, and cell tropism *in vivo*. Commonly, virus-infected tissues are analyzed using conventional immunohistochemistry in paraffin-embedded thin sections. Here, we demonstrate the utility of volumetric three-dimensional (3D) immunofluorescence imaging using tissue optical clearing and light sheet microscopy to investigate host-pathogen interactions of pandemic SARS-CoV-2 in ferrets at a mesoscopic scale. The superior spatial context of large, intact samples (> 150 mm^3) allowed detailed quantification of interrelated parameters like focus-to-focus distance or SARS-CoV-2-infected area, facilitating an in-depth description of SARS-CoV-2 infection foci. Accordingly, we could confirm a preferential infection of the ferret upper respiratory tract by SARS-CoV-2 and emphasize a distinct focal infection pattern in nasal turbinates. Conclusively, we present a proof-of-concept study for investigating critically important respiratory pathogens in their spatial tissue morphology and demonstrate the first specific 3D visualization of SARS-CoV-2 infection.

keywords: SARS-CoV-2, COVID-19, 3D immunofluorescence, light sheet microscopy, confocal laser scanning microscopy, tissue optical clearing, host-pathogen interactions, respiratory tract infection

Introduction

In December 2019, a novel coronavirus (2019-nCoV) associated with viral pneumonia emerged in Wuhan, Hubei Province, China [1-4]. The virus was subsequently designated as severe acute respiratory syndrome coronavirus 2 (SARS-CoV-2) [5] and identified to be the causative agent of COVID-19 (Coronavirus disease 2019). Patients most commonly present with fever, cough, fatigue, and dyspnea [6-9]. About one out of five patients develops severe disease [10,11]. The outbreak was declared a “public health emergency of international concern” on January 30, 2020, and a pandemic on March 11, 2020. As of October 12, 2020, 37,109,851 confirmed cases and 1,070,355 confirmed death were reported in 235 countries [12].

SARS-CoV-2 is an enveloped virus with a single-stranded RNA genome of positive polarity and has been classified as a member of the *Coronaviridae* family, genus *Betacoronavirus* [5]. Including SARS-CoV-2, there are currently two alpha- and five betacoronaviruses associated with human disease [13]. While most result in only mild respiratory illness, the three zoonotic betacoronaviruses SARS-CoV [14], SARS-CoV-2 [1-4], and MERS-CoV [15] (Middle East respiratory syndrome coronavirus) can cause severe respiratory disease. Bats presumably serve as natural reservoir for both SARS-CoV [16,17] and MERS-CoV [18-20], whereas palm civets [21] and dromedary camels [22] have been identified as the intermediate hosts for animal-human transmission for SARS-CoV and MERS-CoV, respectively. Viruses closely related to SARS-CoV-2 have been found in bats [2] and Malayan pangolins [23,24] but no direct transmission event or intermediate host species have been identified thus far.

Over the course of the current pandemic, tremendous research efforts have been undertaken to study the virus and its disease. Consequently, critical information on the virus, e.g. receptor usage [25], and necessary research tools, including reverse genetics systems [26,27], became rapidly available. Furthermore, a variety of animal studies to investigate susceptibility and suitability as animal models have been conducted in a number of animal species (reviewed in [28]): ferrets [29-31], hamsters [32-34], cats [31,35], dogs [31], raccoon dogs [36], rabbits [37], transgenic mice [38-40], pigs [30,31], cattle [41], monkeys [42-44], poultry [30,31,45], and fruit bats [30].

Within the respiratory tract, detection of viral antigen and RNA suggested a preferential replication of SARS-CoV-2 in the upper respiratory tract (URT) of ferrets [29-31], whereas viral antigen was detected in both the URT und lower respiratory tract (LRT) of Syrian hamsters [32,33]. In humans and non-human primates (NHPs), viral antigen detection indicates virus replication in both the URT and LRT [42,46,47].

Thus far, almost all approaches to detect and image SARS-CoV-2 infection in tissues have been based on conventional immunohistochemistry (IHC) of paraffin-embedded thin sections. However, by omitting the spatial context, thin tissue sections of only several micrometers in thickness bear the risk of incomplete or inaccurate description, particularly for focal infections. Recent developments in the field of tissue optical clearing (TOC) have facilitated the preservation of large intact tissue structures by turning them optically transparent. This eliminates the need of physical sectioning and allows acquisition of intact three-dimensional (3D) structures using only optical sectioning, e.g. in light sheet fluorescence microscopy (LSFM) (reviewed in [48]). Lately, the opportunities and advantages of TOC for virus research have been demonstrated in several studies [49-54]. While two approaches to 3D imaging of SARS-CoV-2-infected lung tissue have been described recently [55,56], neither of them is capable of direct visualization of SARS-CoV-2 infection via virus-specific antigen staining.

In our study, we provide a first complete 3D overview of SARS-CoV-2 infection in the ferret model. By staining for the viral nucleocapsid protein (SARS-CoV-2 N), we were able to directly visualize and localize SARS-CoV-2-infected foci within large volumes of the ferret respiratory tract. Direct visualization further allowed detailed description of the foci in their spatial context. To the best of our knowledge, this is the first report of specific 3D reconstruction of SARS-CoV-2 infection as well as the first report of 3D visualization of respiratory virus infection in nasal turbinates using LSFM.

Materials and Methods

Cells and viruses

VeroE6 cells (CCLV-RIE 0929, Collection of Cell Lines in Veterinary Medicine [CCLV], Friedrich-Loeffler-Institut, Germany) were maintained in Minimal Essential Medium (Gibco, USA) supplemented with 10% fetal bovine serum (Biowest, France) and non-essential amino acids (Gibco).

SARS-CoV-2 isolate 2019_nCoV Muc-IMB-1 (kindly provided by Roman Wölfel, German Armed Forces Institute of Microbiology, Germany) was propagated on VeroE6 cells. The complete sequence is available through GISAID under the accession number ID_EPI_ISL_406862 and name "hCoV-19/Germany/BavPat1/2020".

Antibodies and chemical reagents

For the detection of SARS-CoV-2 infection, a 1:1 mixture of hybridoma cell culture supernatants of anti-SARS-CoV-1 N mouse monoclonal antibody clones 4E10A3A1 (RRID:AB_2833160) and 4F3C4 (RRID:AB_2833162) [57] at a dilution of 1:5 or a polyclonal rabbit anti-SARS-CoV-1 N (RRID:AB_838838; Novus Biologicals, USA) at a dilution of 1:250 were used. Alexa Fluor™ 488/568/647-conjugated antibodies against mouse IgG and rabbit IgG were used as secondary antibodies (1:500; Invitrogen, USA).

A detailed list of the chemicals and reagents used for the immunostaining and optical clearing of SARS-CoV-2-infected tissue samples, and their suppliers is provided in Supplementary Table S1.

Virus infection and immunofluorescence staining of mammalian cell cultures

5×10^5 VeroE6 cells were seeded on coverslips one day prior to infection with 1×10^6 $TCID_{50}$ of SARS-CoV-2 isolate 2019_nCoV Muc-IMB-1. Infected VeroE6 cells were then fixed 24 h post-infection with 4% paraformaldehyde (PFA) for 20 min. Following permeabilization with 0.5% Triton X-100/PBS for 15 min, cells were blocked with 10% normal donkey serum in 0.1% Tween-20/PBS (PBS-T) for 30 min. Primary antibodies against SARS-CoV N were applied for 1 h at room temperature in 1% normal donkey serum/PBS-T, followed by three washes with PBS and incubation with the secondary antibody for 1 h at room temperature in 1% normal donkey serum/PBS-T. Nuclei were counterstained with Hoechst33342 (Invitrogen) and samples were embedded in ProLong™ Glass AntiFade Mountant (Invitrogen) for analysis by confocal laser-scanning microscopy.

Tissue samples of SARS-CoV-2-infected ferrets

In a previous study on experimental transmission of SARS-CoV-2 among different animal species, ferrets were inoculated intranasally with 10^5 $TCID_{50}$ of SARS-CoV-2

isolate 2019_nCoV Muc-IMB-1 [30]. Tissues were collected in 10% neutral-buffered formalin and fixed for at least 21 days to ensure complete virus inactivation. In this study, nasal conchae, trachea, and lung tissue samples from infected ferrets euthanized on day 4 post-infection were analyzed.

Immunofluorescence staining of high-volume tissue sections

Large sections of respiratory tissues (≥ 150 mm^3) were immunostained according to a modified iDISCO protocol [50,58]. All incubation steps were conducted with slight agitation and, if not indicated otherwise, at room temperature.

To this end, formaldehyde-fixed tissues were washed three times for at least 1 h each in PBS. Nasal conchae were furthermore decalcified for 4-7 days in Formical-2000™ (Statlab, USA). Samples were trimmed to the sizes and volumes described above, and bleached overnight in 5% H_2O_2 in PBS at 4 °C. For permeabilization, the tissue samples were first incubated twice for 3 h each with 0.2%Triton X-100/PBS at 37 °C and subsequently in 0.2% Triton X-100/20% DMSO/0.3 M glycine/PBS for 2 days at 37 °C. Following a blocking step with 6% normal donkey serum/0.2% Triton X-100/10% DMSO/PBS for 2 days at 37 °C, primary antibodies were diluted in 3% normal donkey serum/5% DMSO in PTwH (0.2% Tween-20 in PBS with 10 µg/mL heparin) and applied for 4 days at 37 °C. Unbound antibody was removed by washing the samples 4-5 times over the course of a day, leaving the final wash on overnight. Secondary antibodies were diluted in 3% normal donkey serum/PTwH and the samples were incubated for another 4 days at 37 °C. Washing was performed as described for the primary antibody.

Ethyl cinnamate (ECi)-based tissue optical clearing

Immunostained tissue sections were cleared with an adjusted ECi-based protocol [59]. All incubation steps were conducted with slight agitation.

The samples were dehydrated in a graded ethanol series (30% [v/v], 50%, 70%, and twice in 100%; each for ≥ 8 h at 4 °C, diluted in aqua ad iniectabilia, and pH-adjusted to 9). Following a two-hour wash with *n*-hexane at room temperature [60], *n*-hexane was gradually replaced with the clearing agent ECi and samples were incubated until optically transparent.

Light sheet microscopy of optically clear tissue samples

Light sheet micrographs of optically clear and immunostained respiratory tissues from SARS-CoV-2-infected ferrets were acquired with a LaVision BioTec Ultramicroscope II (LaVision, Germany). The microscope was equipped with an Olympus MVX-10 zoom body (magnification range: 0.63x – 6.3x, total magnification: 1.26x – 12.6x; Olympus, Japan), an Olympus MVPLAPO 2x objective (NA = 0.5), a LaVision laser module with four laser lines (488 nm, 561 nm, 639 nm, and 785 nm), and a Andor Zyla 5.5 sCMOS Camera (Andor Technology, UK) with a pixel size of 6.5 μm^2. To visualize tissue morphology, non-specific autofluorescence was excited with the 488 nm laser. Excitation lines 561 nm and 639 nm were used to excite Alexa Fluor™ 568 and Alexa Fluor™ 647, respectively. Channels of a high-volume 3D image were acquired sequentially with a z-step size of 2 µm, a light sheet width of 100%, and a light sheet thickness of 3.89 µm (NA = 0.156). Acquisition was done with ImSpector (v7.0.124.0).

Confocal laser-scanning microscopy (CLSM)

Confocal images were acquired with a Leica DMI6000 TCS SP5 confocal laser-scanning microscope (Leica Microsystems, Germany) equipped with a 63x/1.40 oil immersion HCX PL APO objective and a 40x/1.10 water immersion HC PL APO objective. Fluorescence was recorded sequentially between lines with a pinhole diameter of 1 Airy unit and z-step sizes of 0.35 µm. Acquisition was done with LAS AF (v2.7.3.9723).

For high-resolution confocal laser-scanning analysis of cleared and immunostained tissue samples, they were sectioned into 1-mm-thick slices using a stainless steel tissue matrix (World Precision Instruments, UK). Tissue slices were then mounted in 3D-printed imaging containers as described before [50]. Tissue morphology was reconstructed from non-specific tissue autofluorescence via excitation with a 405 nm UV laser diode.

Image processing and analysis

Image visualization and analysis were performed with arivis Vision4D (v3.2). If necessary, channels were background corrected. CLSM-acquired image stacks of subsectioned volumetric tissue samples were denoised. To quantify relations between SARS-CoV-2 infection foci, they were segmented. The shortest distances between foci were measured using the segment operation “Distances”. To calculate

the area of SARS-CoV-2-infected tissue, surface areas of the segmented objects were extracted and divided by two to account only for the surface of the object facing outwards. Lookup tables of multicolor images were selected for maximum accessibility.

Results

LSFM provides a unique insight into the spatial distribution of SARS-CoV-2 in intact nasal turbinates. By combining LSFM with optically cleared samples of the ferret respiratory tract (Figure 1A), we aimed to shed light on the infection environment and spatial context of SARS-CoV-2 infection. A commercially available polyclonal serum (designated as #1), which has been used for SARS-CoV-2 detection by conventional IHC [30,42], and a mix of two monoclonal antibodies (designated as #2) against SARS-CoV N were tested on virus-infected VeroE6 cells and confirmed to be cross-reactive with SARS-CoV-2 N (Figure 1B). Following immunostaining, ferret tissue samples, including the partly ossified nasal conchae, were successfully turned optically transparent using a recently established ethyl cinnamate (ECi)-based approach [59] (Figure 1C).

Full translucency of ferret nasal turbinates enabled LSFM acquisition of a > 200 mm^3 (6.69 gigavoxels per channel; $\sum$ = 20.07 gigavoxels)-sized tissue sample (Figure 2A and Supplementary Movie S1). While there were some unspecific signals detectable in the SARS-CoV-2 N-stained sample (individual green or magenta spots), they could be clearly distinguished from specific SARS-CoV-2 detection by the absence of colocalization (white) of the signals from either antibody (Figure 2B and Figure S1). Within the about 4-mm-thick URT sample (4 days post-infection), multiple comparatively small SARS-CoV-2 infection hot spots were visualized (Figure 2B). They were detected in both the *Concha nasalis dorsalis* (Figure 2B, ROIs [region of interests] 1 & 2) and the *Concha nasalis ventralis* (Figure 2B, ROI 3). Overall, these data provide the proof of concept for the feasibility of TOC-assisted LSFM analysis for SARS-CoV-2.

SARS-CoV-2 infection in the upper respiratory tract of ferrets is characterized by an oligofocal infection pattern. To achieve a more in-depth analysis of the individual SARS-CoV-2 infection foci, LSFM image stacks of infected areas were acquired using a higher magnification (total magnification of 8x for Figure 3 vs. 1.26x

for Figure 2), thus, increasing image resolution while maintaining the complete spatial context (Figure 3).

Virtually traveling through an image stack of the ROIs 1 & 2 from Figure 2, which was acquired accordingly, corroborated the presence of three individual, well delimitable, and distinguishable SARS-CoV-2 infection foci (Figure 3A, images 1 [filled-in arrowhead], 5 [outlined arrowhead], and 7 [arrow]). A volumetric reconstruction of this image stack was able to convey spatial relationships between the individual infection spots (Figure 3B-D). Specificity of SARS-CoV-2 N detection was again confirmed by colocalization of both independent antibody stainings (Figure 3B and C, right side). Consequently, linear distances between foci and foci areas were quantified (Figure 4 and Table 1). This increased spatial context within the nasal turbinate sample is further reinforced by the fact that the SARS-CoV-2 infection focus from Figure 3A7 (arrow) is buried deeper within the sample and cannot be seen from the frontal angle in Figure 3B. However, either by virtually clipping the sample as indicated (Figure 3B and C, red square) or using 3D rendering to virtually “fly through the sample” (Supplementary Movie S2), the infection site can be visualized. Taken together, this emphasizes the system’s flexibility to switch from broad, mesoscopic overviews to detailed, resolved close-ups. By maintaining the full infection environment, we were able to establish quantifiable relations between the individual SARS-CoV-2 foci and highlight the oligofocal infection pattern of SARS-CoV-2 in the URT of ferrets.

Table 1: Direct linear distances between, areas affected by, and volumes of segmented SARS-CoV-2 infection foci. Linear distances were calculated either as the distance between the center of two foci or as the shortest possible distance between the edges of two foci. The area affected by SARS-CoV-2 infection was measured by calculating the surface area of the segmented objects and dividing the resultant value by two, thus, only accounting for the surface facing outwards.

linear distance [µm]		A1	A5	A7
from the center	A1	0	777.4	1303.3
	A5	777.4	0	554.3
	A7	1303.3	554.3	0
from the edge	A1	0	421.1	997.5
	A5	421.1	0	75.5

	A7	997.5	75.5	0
area [µm^2]		90,212	75,389	181,431
volume [µm^3]		465,818	443,207	1,533,316

CLSM acquisition of correlated regions of interest at subcellular resolution – infection of ciliated and non-ciliated cells in the nasal epithelium. While LSFM is ideally suited to generate a mesoscopic overview to analyze, for example, large-scale spatial virus distribution within virus-infected tissues, simultaneous resolution of subcellular details is not possible. Thus, following LSFM acquisition, we subsectioned the optically cleared high-volume tissue sample to 1-mm thick slices using a tissue matrix to achieve compatibility with the limited free working distances of CLSM objectives (Figure 1A).

Using the spatio-morphological information on the distribution of SARS-CoV-2 infection foci obtained from LSFM analysis, high-resolution CLSM image stacks of a SARS-CoV-2 infection focus in the *Concha nasalis dorsalis* (ROI 1 from Figure 2) were acquired (Figure 5). Individual SARS-CoV-2-infected cells could be resolved, demonstrating cytoplasmic SARS-CoV-2 N distribution in both ciliated and non-ciliated cells (Figure 5B, arrows). Notably, SARS-CoV-2 N accumulated particularly at the apical side of the ciliated cells. Overall, these data demonstrate the feasibility of this correlated approach to dissect cell-specific responses to SARS-CoV-2 infection *in vivo* at subcellular resolution.

SARS-CoV-2 detection in the LRT of ferrets. Previous studies demonstrated a preferential replication of SARS-CoV-2 in the URT of ferrets [29-31]. To assess whether comprehensive LSFM analysis may uncover previously undetected SARS-CoV-2 infection foci in the LRT, we looked at optically cleared high-volume lung and tracheal samples.

As before, some unspecific fluorescence signals could be seen in both lung (Figure 6) and tracheal tissue (Figure S2 and Supplementary Movie S3). At a first glance, no specific SARS-CoV-2 infection foci could be identified. However, hidden within an airway of the large lung tissue volume, a 172 µm by 102 µm-sized spot of colocalized antibody signals was detected (Figure 6B and Supplementary Movie S4). Contrary to the SARS-CoV-2 infection foci in the ferret nasal turbinates (Figures 2 and 3), the

signal was localized above the epithelial cell layer (Figure 6B, single plane). This suggested detection of debris-associated antigen, which was mostly likely inhaled from the URT. Overall, while we were able to detect an $8.6x10^{-5}$ mm^3 (86,000 μm^3) spot of debris-associated antigen within a > 80 mm^3 volume, we did not identify additional sites of infection within the LRT of ferrets, which corroborates preferential replication of SARS-CoV-2 in the URT of ferrets.

Discussion

While conventional immunohistochemistry studies have been used to assess the presence or absence of SARS-CoV-2 antigen in human and animal tissues [29-33,42,46,47], none of them were able to provide a greater spatial context of the infection site. By combining TOC with LSFM, we acquired large intact volumes of SARS-CoV-2-infected respiratory tissues from ferrets (Figure 1). The direct 3D visualization of virus infection via SARS-CoV-2 N staining established a comprehensive and mesoscopic overview of the infection in its full spatial context (Figures 2-6 and Supplementary Movies 1-4). Moreover, the determination of morphological parameters, e.g. focus-to-focus distances or the area of virus-infected tissue, not only allowed the characterization of individual SARS-CoV-2 infection foci but also provided a first quantitative insight into virus distribution within the spatio-morphological context of ferret nasal turbinates (Figure 4 and Table 1).

Here, we employed an ECi-based TOC approach [59] and adjusted it to visualize immunostained SARS-CoV-2 infection in large tissue samples of the respiratory tract of ferrets. While two 3D imaging approaches to SARS-CoV-2 infection in lung tissue have been reported, they have an entirely different scope: as both represent virtual histopathology strategies, they are meant to assess pathophysiology and associated tissue damage, but inherently cannot map and visualize specific SARS-CoV-2 infection. For the first study, Eckermann et al. [55] developed and demonstrated the utility of a phase contrast x-ray tomography concept to investigate unstained lung tissue. The second study describes the use of fluorescent H&E-analog stains (TO-PRO-3 for nuclear contrast and Eosin-Y for cytoplasmic/stromal contrast) to achieve “3D pseudo-histological imaging” [56]. Consequently, our study constitutes the first report of direct 3D visualization of SARS-CoV-2 infection via LSFM. While unspecific antibody signals were detected for both the polyclonal serum and the monoclonal mix directed against N of SARS-CoV, particularly on the outer surface of the tissue

blocks, specificity for SARS-CoV-2 was ensured via colocalization of either staining (Figures 2, 3, 5, and 6) and absence of colocalization in naïve animals (Figure S1). Further optimization of the immunostaining protocol or the availability of SARS-CoV-2-specific antibodies will likely aid in reduction of background staining and improvement of virus detection.

In addition to the specific 3D reconstruction of SARS-CoV-2 infection within its spatio-morphological environment, the implementation of quantitative image analysis following accurate quantification of interrelated 3D parameters (Figure 4 and Table 1) represents a pronounced advantage of 3D immunofluorescence imaging over conventional IHC. To achieve a somewhat comparable yet more artifact-prone 3D reconstruction from thin sections, exceedingly laborious and time-consuming image registration pipelines following serial thin sectioning are necessary [61]. For instance, the nasal turbinate section from Figures 2-4 alone would require processing of around 800 sections (at 5 µm thickness), making it de facto impossible with 2D IHC.

When compared to previous studies [29-31], the spatial visualization of SARS-CoV-2 in the ferret respiratory tract confirmed preferential infection of the URT (Figures 2-4). Furthermore, our data indicate and emphasize a distinct oligofocal infection pattern of SARS-CoV-2 within nasal turbinates (Figures 2-4). Within a > 200 mm^3 section of nasal turbinate tissue, only four SARS-CoV-2 infection foci (with a combined volume of $5.17x10^{-3}$ mm^3) were detected, three of which accumulated in the *Concha nasalis dorsalis* and exhibited a maximum linear distance of 1.3 mm to each other (Figure 4 and Table 1). It is important to note that tissues inevitably shrink during the fixation, dehydration, and clearing process. For the EtOH-ECi-based TOC approach used here, a 50% volume reduction, equaling to a change of about 20% in tissue diameters, has been determined [59]. The limited degree of infection is particularly interesting in view of the amounts of infectious virus and genome copies that can be isolated from the URT of ferrets [29-31] and other animal species, like Syrian hamsters [32-34] and rhesus macaques [42-44]. Clustering of SARS-CoV-2 infection foci in narrow areas of the URT might also have implications for the likelihood of isolation of infectious virus and the detection of viral RNA from nasal swabs in comparison to nasal washes from ferrets and possibly other animal models. Accordingly, a high degree of variation in viral copy numbers can be observed from nose or throat swabs in comparison to bronchoalveolar lavages from SARS-CoV-2-

infected rhesus macaques [42]. However, because of the proof-of-principle character of our study and the limited availability of SARS-CoV-2-infected material, further studies have to corroborate the clustering and focal infection pattern of SARS-CoV-2 in the URT.

Alongside complex quantitative 3D image analysis, volumetric imaging has the potential to discover rare events, as demonstrated by the detection of cancer metastases in sentinel lymph nodes, which had not been found via conventional IHC [62]. While preferential replication of SARS-CoV-2 in the URT of ferrets has been demonstrated via viral RNA and antigen detection [29-31], Kim et al. also detected some SARS-CoV-2-positive cells in the LRT. This is in contrast to the two other ferret susceptibility studies, which detected either no [31] or only low amounts [30] of viral RNA in the LRT, but neither found any SARS-CoV-2 antigen at this location. It is conceivable that scarce LRT infection had been overlooked in previous 2D IHC studies because of the focal character of SARS-CoV-2 infection in the tissue or that the detected viral RNA originated from URT-derived aspirated material. Using this high-volume imaging approach, we aimed to screen the tissue for rare SARS-CoV-2 infection foci in the LRT. While we did not detect any infection spots in tracheal tissue (Figure S2), we did visualize an individual, only 86,000 µm^3-sized SARS-CoV-2 N-positive structure inside a lung airway (Figure 6B). However, spatial analysis revealed that the signal, contrary to the SARS-CoV-2 infection foci in the nasal turbinate epithelium (Figures 2 and 3), was detected above the airway epithelial layer. This strongly suggested that the structure most likely represents aspirated virus-containing debris as the result of localized cell or tissue damage at infected URT sites. Accordingly, this example emphasizes the suitability of this volumetric 3D LSFM approach to identify rare and highly localized pathogen-related events.

Ferrets are a standard model for human respiratory infection (reviewed in [63]). However, they recapitulate only mild SARS-CoV-2 infection and do not develop severe respiratory disease [11,29-31]. In contrast, both URT and LRT are strongly affected by SARS-CoV-2 infection in Syrian hamsters, including overt signs of disease [32,33]. This is closer to human disease, where SARS-CoV-2 antigen is found in the URT and LRT, as corroborated by the NHP model rhesus macaques [42-44]. While this proof-of-principle study is focused on ferret samples, it may serve as

392 blueprint for further analyses in other animal models and even human clinical
393 samples.

394 Independent of sample origin, volumetric imaging of cleared samples enables
395 discovery and detection of rare infection events, as demonstrated earlier. This
396 facilitates the investigation of the involvement of other organs outside of the
397 respiratory tract in SARS-CoV-2 infection. For instance, viral antigen has been
398 detected in the intestine of ferrets [29], hamsters [32,33], and rhesus macaques [42].
399 While viral RNA has been detected in human clinical brain samples [64], infection of
400 cells of the central nervous system could thus far only be demonstrated
401 experimentally in 3D human brain organoids [65]. Except for genetically modified
402 mice expressing human angiotensin-converting enzyme 2 (ACE2) [39], the presence
403 of SARS-CoV-2 antigen in animal or human brain samples has yet to be shown.
404 Previous studies with other viral pathogens demonstrated that volumetric 3D imaging
405 using TOC and LSFM is a highly valuable tool to assess the comprehensive
406 distribution of virus infection *in vivo* [49,52]. Additional immunostaining against tissue-
407 specific cell markers may further facilitate the investigation of the global SARS-CoV-2
408 cell tropism in affected tissues. Combining and correlating this with high-resolution
409 CLSM analysis of SARS-CoV-2 hot spots identified via LSFM has the potential to
410 dissect subcellular infection processes of SARS-CoV-2 *in vivo* with unparalleled
411 detail. These results form the basis for research on larger sample sizes of both
412 respiratory and non-respiratory tissues from SARS-CoV-2 animal models and human
413 clinical samples using volumetric 3D LSFM of immunostained and cleared tissues.

414 Overall, we demonstrate the proof of concept for the utility of volumetric 3D
415 immunofluorescence of critically important respiratory pathogens like SARS-CoV-2
416 using TOC and LSFM. The ability to analyze interrelated morphological parameters,
417 like inter-foci distances and SARS-CoV-2-affected areas, and to put them into global
418 perspective to the spatial tissue morphology provides unprecedented insight into
419 SARS-CoV-2 infection in the respiratory tract of ferrets. In the future, this approach
420 will be a crucial tool to understand the mesoscopic scale of host-pathogen
421 interactions of SARS-CoV-2 but also other respiratory and non-respiratory
422 pathogens, including, for example, influenza A and henipaviruses.

423 ## Author contributions

Conceptualization, L.M.Z. and S.F.; methodology, L.M.Z.; formal analysis, L.M.Z.; investigation, L.M.Z., D.S. and M.M.; resources, J.S., D.H., M.B. and A.B.; writing—original draft preparation, L.M.Z. and S.F.; writing—review and editing, L.M.Z., D.S., J.S., M.M., D.H., M.B., E.M.A., T.C.M., A.B. and S.F.; visualization, L.M.Z.; supervision, E.M.A. and S.F.; project administration, S.F.; funding acquisition, S.F and T.C.M.

Acknowledgments

We thank Roman Wölfel (German Armed Forces Institute of Microbiology, Germany) for providing the SARS-CoV-2 isolate and Sven Reiche (Friedrich-Loeffler-Institut, Germany) for providing the SARS-CoV N monoclonal antibodies. We are grateful to Angela Hillner for excellent technical assistance. Figure 1A was created with Biorender.com.

Funding

The study was supported by intramural funding of the German Federal Ministry of Food and Agriculture provided to the Friedrich-Loeffler-Institut. L.M.Z was supported by the Federal Excellence Initiative of Mecklenburg-Western Pomerania and European Social Fund (ESF) Grant KoInfekt (ESF/14-BM-A55-0002/16).

Conflict of Interest

The authors declare no competing interests.

Figure legends

Figure 1: Workflow for correlative LSFM-CLSM of SARS-CoV-2-infected ferret tissues. (A) Nasal conchae and lungs tissue from SARS-CoV-2-infected ferrets were collected, trimmed, and immunostained against SARS-CoV-2 N protein. Fully dehydrated and optically transparent samples were acquired *in toto* with a light sheet microscope and subsequently subsectioned to 1 mm-thick sections for correlative confocal laser-scanning microscopy. **(B)** Representative immunostaining for SARS-CoV-2 N in infected VeroE6 cells using a commercially available polyclonal anti-SARS-CoV N serum (#1, green) and a monoclonal anti-SARS-CoV N mix (#2, magenta) confirms antibody specificity. Blue: Hoechst33342. Scale bars = 15 µm. **(C)** Representative ferret respiratory tract samples before (left) and after (right)

454 immunostaining and ECi-based optical clearing. The photographs from the lung
455 sections (bottom) show two independent samples. Edge length of grid square: 1 mm.

456 **Figure 2: LSFM is able to visualize SARS-CoV-2 infection in nasal turbinates**
457 **within a high spatial context. (A)** The tissue structure of the nasal conchae (> 200
458 mm^3; 4 days post-infection) was reconstructed using tissue autofluorescence (cyan)
459 and is depicted as volumetric projection from three viewing angles. Anatomical terms
460 of location are provided for orientation. Edge length of grid squares = 2 mm. Total
461 magnification = 1.26x. **(B)** Maximum intensity projections of the regions of interest (1-
462 3) highlighted in (A). SARS-CoV-2 infection is characterized by colocalization of both
463 SARS-CoV-2 N stainings (#1, green; #2, magenta) and results in white coloring
464 (inset). Four distinct SARS-CoV-2 infection foci are highlighted (filled-in arrowhead
465 [A1], outlined arrowhead [A5], arrow [A7], and asterisk). Foci will hereafter be
466 referred to via their respective indicator or designation in square brackets. Ranges of
467 the MIPs in the *z*-dimension are provided above the respective image. MIP =
468 maximum intensity projection. Scale bar = 1 mm.

469 **Figure 3: 3D detail views highlight oligofocal SARS-CoV-2 infection pattern in**
470 **nasal turbinates at 4 days post-infection. (A)** Tomographic representation of three
471 individual SARS-CoV-2 foci (filled-in arrowhead [A1], outlined arrowhead [A5], and
472 arrow [A7]) from ROIs 1 & 2 in Figure 2 along a length of 1,658 µm. The relative
473 distance to plane #1 is indicated in the bottom left corner. Cyan = autofluorescence;
474 green = SARS-CoV-2 N #1; magenta = SARS-CoV-2 N #2. Scale bar = 400 µm.
475 Total magnification = 8x. **(B,C)** Volumetric projections of the detail view from two
476 angles. Clipping at the indicated plane (red) reveals the third SARS-CoV-2 foci (C,
477 arrow), which is hidden behind nasal turbinate tissue in (B). Single channel views
478 further emphasize the colocalizing pattern of both SARS-CoV-2 N stainings (#1,
479 green; #2, magenta). Cyan/grayscale = autofluorescence (AF). **(D)** Close-ups of the
480 three individual infection foci. The angle of the respective image is indicated in the
481 bottom left corner.

482 **Figure 4: Virtual segmentation of SARS-CoV-2 infection foci at 4 days post-**
483 **infection**. **(A)** xz-view of the magnified nasal turbinate view from Figure 3, clipped at
484 the indicated plane (red square). Segmented SARS-CoV-2 infection foci (A1: yellow,
485 A5: red; A7: light blue) are visible through the autofluorescence reconstruction of the
486 tissue morphology (cyan). Once they are uncovered by the clipping plane, they are

highlighted with their respective indicator. **(B)** Detail and alternate viewing angle of segmented infection foci. A slightly darker sphere represents the respective foci center. The direct linear distances between the centers of each foci (from Table 1) are highlighted.

Figure 5: High-resolution CLSM analysis of SARS-CoV-2 infection foci in the concha nasalis dorsalis of a SARS-CoV-2-infected ferret at 4 days-post infection. (A) 3D maximum intensity projection (MIP) of a SARS-CoV-2 infection focus from ROI 1 in Figure 2. The image stack was acquired with a 40x/1.1 water immersion objective. Cyan = autofluorescence; green = SARS-CoV-2 N #1; magenta = SARS-CoV-2 N #2. Edge length of grid square = 40 µm. **(B)** MIPs from ROIs 1 and 2 in (A). Individual cells can be analyzed at subcellular resolution, highlighting infection of ciliated and non-ciliated cells (arrows). Scale bar = 100 µm (overview) and 5 µm (detail).

Figure 6: Only debris-associated SARS-CoV-2 antigen was detectable in ferret lung tissue at 4 days post-infection. (A) Volumetric projection of a large lung tissue section. While some background staining is detectable for the monoclonal antibody mix (#2, magenta), no signal overlap with the polyclonal antibody (#1, green) is visible. Cyan/grayscale = autofluorescence. Edge length of grid squares = 800 µm. Total magnification = 1.6x. **(B)** Alternate viewing angles reveal a spot inside an airway where both signals colocalize (white box in (A)). Contrary to the SARS-CoV-2-associated foci in Figures 2 and 3, the overlapping signal is detected lying on top the epithelial layer, suggesting that it is most likely cell debris inhaled from the URT.

References

1. Zhu, N.; Zhang, D.; Wang, W.; Li, X.; Yang, B.; Song, J.; Zhao, X.; Huang, B.; Shi, W.; Lu, R., et al. A Novel Coronavirus from Patients with Pneumonia in China, 2019. *N Engl J Med* **2020**, *382*, 727-733, doi:10.1056/NEJMoa2001017.
2. Zhou, P.; Yang, X.L.; Wang, X.G.; Hu, B.; Zhang, L.; Zhang, W.; Si, H.R.; Zhu, Y.; Li, B.; Huang, C.L., et al. A pneumonia outbreak associated with a new coronavirus of probable bat origin. *Nature* **2020**, *579*, 270-273, doi:10.1038/s41586-020-2012-7.
3. Wu, F.; Zhao, S.; Yu, B.; Chen, Y.M.; Wang, W.; Song, Z.G.; Hu, Y.; Tao, Z.W.; Tian, J.H.; Pei, Y.Y., et al. A new coronavirus associated with human respiratory disease in China. *Nature* **2020**, *579*, 265-269, doi:10.1038/s41586-020-2008-3.

4. Wang, C.; Horby, P.W.; Hayden, F.G.; Gao, G.F. A novel coronavirus outbreak of global health concern. *Lancet* **2020**, *395*, 470-473, doi:10.1016/S0140-6736(20)30185-9.
5. Coronaviridae Study Group of the International Committee on Taxonomy of, V. The species Severe acute respiratory syndrome-related coronavirus: classifying 2019-nCoV and naming it SARS-CoV-2. *Nat Microbiol* **2020**, *5*, 536-544, doi:10.1038/s41564-020-0695-z.
6. Chen, N.; Zhou, M.; Dong, X.; Qu, J.; Gong, F.; Han, Y.; Qiu, Y.; Wang, J.; Liu, Y.; Wei, Y., et al. Epidemiological and clinical characteristics of 99 cases of 2019 novel coronavirus pneumonia in Wuhan, China: a descriptive study. *Lancet* **2020**, *395*, 507-513, doi:10.1016/S0140-6736(20)30211-7.
7. Zhou, F.; Yu, T.; Du, R.; Fan, G.; Liu, Y.; Liu, Z.; Xiang, J.; Wang, Y.; Song, B.; Gu, X., et al. Clinical course and risk factors for mortality of adult inpatients with COVID-19 in Wuhan, China: a retrospective cohort study. *Lancet* **2020**, *395*, 1054-1062, doi:10.1016/S0140-6736(20)30566-3.
8. Guan, W.J.; Ni, Z.Y.; Hu, Y.; Liang, W.H.; Ou, C.Q.; He, J.X.; Liu, L.; Shan, H.; Lei, C.L.; Hui, D.S.C., et al. Clinical Characteristics of Coronavirus Disease 2019 in China. *N Engl J Med* **2020**, *382*, 1708-1720, doi:10.1056/NEJMoa2002032.
9. Huang, C.; Wang, Y.; Li, X.; Ren, L.; Zhao, J.; Hu, Y.; Zhang, L.; Fan, G.; Xu, J.; Gu, X., et al. Clinical features of patients infected with 2019 novel coronavirus in Wuhan, China. *Lancet* **2020**, *395*, 497-506, doi:10.1016/S0140-6736(20)30183-5.
10. Yang, Y.; Xiao, Z.; Ye, K.; He, X.; Sun, B.; Qin, Z.; Yu, J.; Yao, J.; Wu, Q.; Bao, Z., et al. SARS-CoV-2: characteristics and current advances in research. *Virol J* **2020**, *17*, 117, doi:10.1186/s12985-020-01369-z.
11. Johansen, M.D.; Irving, A.; Montagutelli, X.; Tate, M.D.; Rudloff, I.; Nold, M.F.; Hansbro, N.G.; Kim, R.Y.; Donovan, C.; Liu, G., et al. Animal and translational models of SARS-CoV-2 infection and COVID-19. *Mucosal Immunol* **2020**, 10.1038/s41385-020-00340-z, doi:10.1038/s41385-020-00340-z.
12. WHO. Coronavirus disease (COVID-19) Weekly Epidemiological Update, 12 October 2020. Availabe online: https://www.who.int/docs/default-source/coronaviruse/situation-reports/20201012-weekly-epi-update-9.pdf (accessed on 12 October 2020).
13. Cui, J.; Li, F.; Shi, Z.L. Origin and evolution of pathogenic coronaviruses. *Nat Rev Microbiol* **2019**, *17*, 181-192, doi:10.1038/s41579-018-0118-9.
14. Drosten, C.; Gunther, S.; Preiser, W.; van der Werf, S.; Brodt, H.R.; Becker, S.; Rabenau, H.; Panning, M.; Kolesnikova, L.; Fouchier, R.A., et al. Identification of a novel coronavirus in patients with severe acute respiratory syndrome. *N Engl J Med* **2003**, *348*, 1967-1976, doi:10.1056/NEJMoa030747.
15. Zaki, A.M.; van Boheemen, S.; Bestebroer, T.M.; Osterhaus, A.D.; Fouchier, R.A. Isolation of a novel coronavirus from a man with pneumonia in Saudi Arabia. *N Engl J Med* **2012**, *367*, 1814-1820, doi:10.1056/NEJMoa1211721.
16. Lau, S.K.; Woo, P.C.; Li, K.S.; Huang, Y.; Tsoi, H.W.; Wong, B.H.; Wong, S.S.; Leung, S.Y.; Chan, K.H.; Yuen, K.Y. Severe acute respiratory syndrome coronavirus-like virus in Chinese horseshoe bats. *Proc Natl Acad Sci U S A* **2005**, *102*, 14040-14045, doi:10.1073/pnas.0506735102.
17. Li, W.; Shi, Z.; Yu, M.; Ren, W.; Smith, C.; Epstein, J.H.; Wang, H.; Crameri, G.; Hu, Z.; Zhang, H., et al. Bats are natural reservoirs of SARS-like coronaviruses. *Science* **2005**, *310*, 676-679, doi:10.1126/science.1118391.

18. Corman, V.M.; Ithete, N.L.; Richards, L.R.; Schoeman, M.C.; Preiser, W.; Drosten, C.; Drexler, J.F. Rooting the phylogenetic tree of middle East respiratory syndrome coronavirus by characterization of a conspecific virus from an African bat. *J Virol* **2014**, *88*, 11297-11303, doi:10.1128/JVI.01498-14.
19. Lau, S.K.; Li, K.S.; Tsang, A.K.; Lam, C.S.; Ahmed, S.; Chen, H.; Chan, K.H.; Woo, P.C.; Yuen, K.Y. Genetic characterization of Betacoronavirus lineage C viruses in bats reveals marked sequence divergence in the spike protein of pipistrellus bat coronavirus HKU5 in Japanese pipistrelle: implications for the origin of the novel Middle East respiratory syndrome coronavirus. *J Virol* **2013**, *87*, 8638-8650, doi:10.1128/JVI.01055-13.
20. Yang, L.; Wu, Z.; Ren, X.; Yang, F.; Zhang, J.; He, G.; Dong, J.; Sun, L.; Zhu, Y.; Zhang, S., et al. MERS-related betacoronavirus in Vespertilio superans bats, China. *Emerg Infect Dis* **2014**, *20*, 1260-1262, doi:10.3201/eid2007.140318.
21. Guan, Y.; Zheng, B.J.; He, Y.Q.; Liu, X.L.; Zhuang, Z.X.; Cheung, C.L.; Luo, S.W.; Li, P.H.; Zhang, L.J.; Guan, Y.J., et al. Isolation and characterization of viruses related to the SARS coronavirus from animals in southern China. *Science* **2003**, *302*, 276-278, doi:10.1126/science.1087139.
22. Haagmans, B.L.; Al Dhahiry, S.H.; Reusken, C.B.; Raj, V.S.; Galiano, M.; Myers, R.; Godeke, G.J.; Jonges, M.; Farag, E.; Diab, A., et al. Middle East respiratory syndrome coronavirus in dromedary camels: an outbreak investigation. *Lancet Infect Dis* **2014**, *14*, 140-145, doi:10.1016/S1473-3099(13)70690-X.
23. Lam, T.T.; Jia, N.; Zhang, Y.W.; Shum, M.H.; Jiang, J.F.; Zhu, H.C.; Tong, Y.G.; Shi, Y.X.; Ni, X.B.; Liao, Y.S., et al. Identifying SARS-CoV-2-related coronaviruses in Malayan pangolins. *Nature* **2020**, *583*, 282-285, doi:10.1038/s41586-020-2169-0.
24. Xiao, K.; Zhai, J.; Feng, Y.; Zhou, N.; Zhang, X.; Zou, J.J.; Li, N.; Guo, Y.; Li, X.; Shen, X., et al. Isolation of SARS-CoV-2-related coronavirus from Malayan pangolins. *Nature* **2020**, *583*, 286-289, doi:10.1038/s41586-020-2313-x.
25. Hoffmann, M.; Kleine-Weber, H.; Schroeder, S.; Kruger, N.; Herrler, T.; Erichsen, S.; Schiergens, T.S.; Herrler, G.; Wu, N.H.; Nitsche, A., et al. SARS-CoV-2 Cell Entry Depends on ACE2 and TMPRSS2 and Is Blocked by a Clinically Proven Protease Inhibitor. *Cell* **2020**, *181*, 271-280 e278, doi:10.1016/j.cell.2020.02.052.
26. Thi Nhu Thao, T.; Labroussaa, F.; Ebert, N.; V'Kovski, P.; Stalder, H.; Portmann, J.; Kelly, J.; Steiner, S.; Holwerda, M.; Kratzel, A., et al. Rapid reconstruction of SARS-CoV-2 using a synthetic genomics platform. *Nature* **2020**, *582*, 561-565, doi:10.1038/s41586-020-2294-9.
27. Xie, X.; Muruato, A.; Lokugamage, K.G.; Narayanan, K.; Zhang, X.; Zou, J.; Liu, J.; Schindewolf, C.; Bopp, N.E.; Aguilar, P.V., et al. An Infectious cDNA Clone of SARS-CoV-2. *Cell Host Microbe* **2020**, *27*, 841-848 e843, doi:10.1016/j.chom.2020.04.004.
28. Abdel-Moneim, A.S.; Abdelwhab, E.M. Evidence for SARS-CoV-2 Infection of Animal Hosts. *Pathogens* **2020**, *9*, doi:10.3390/pathogens9070529.
29. Kim, Y.I.; Kim, S.G.; Kim, S.M.; Kim, E.H.; Park, S.J.; Yu, K.M.; Chang, J.H.; Kim, E.J.; Lee, S.; Casel, M.A.B., et al. Infection and Rapid Transmission of SARS-CoV-2 in Ferrets. *Cell Host Microbe* **2020**, *27*, 704-709 e702, doi:10.1016/j.chom.2020.03.023.
30. Schlottau, K.; Rissmann, M.; Graaf, A.; Schon, J.; Sehl, J.; Wylezich, C.; Hoper, D.; Mettenleiter, T.C.; Balkema-Buschmann, A.; Harder, T., et al.

SARS-CoV-2 in fruit bats, ferrets, pigs, and chickens: an experimental transmission study. *Lancet Microbe* **2020**, *1*, e218-e225, doi:10.1016/S2666-5247(20)30089-6.

31. Shi, J.; Wen, Z.; Zhong, G.; Yang, H.; Wang, C.; Huang, B.; Liu, R.; He, X.; Shuai, L.; Sun, Z., et al. Susceptibility of ferrets, cats, dogs, and other domesticated animals to SARS-coronavirus 2. *Science* **2020**, *368*, 1016-1020, doi:10.1126/science.abb7015.
32. Chan, J.F.; Zhang, A.J.; Yuan, S.; Poon, V.K.; Chan, C.C.; Lee, A.C.; Chan, W.M.; Fan, Z.; Tsoi, H.W.; Wen, L., et al. Simulation of the clinical and pathological manifestations of Coronavirus Disease 2019 (COVID-19) in golden Syrian hamster model: implications for disease pathogenesis and transmissibility. *Clin Infect Dis* **2020**, 10.1093/cid/ciaa325, doi:10.1093/cid/ciaa325.
33. Sia, S.F.; Yan, L.M.; Chin, A.W.H.; Fung, K.; Choy, K.T.; Wong, A.Y.L.; Kaewpreedee, P.; Perera, R.; Poon, L.L.M.; Nicholls, J.M., et al. Pathogenesis and transmission of SARS-CoV-2 in golden hamsters. *Nature* **2020**, *583*, 834-838, doi:10.1038/s41586-020-2342-5.
34. Osterrieder, N.; Bertzbach, L.D.; Dietert, K.; Abdelgawad, A.; Vladimirova, D.; Kunec, D.; Hoffmann, D.; Beer, M.; Gruber, A.D.; Trimpert, J. Age-Dependent Progression of SARS-CoV-2 Infection in Syrian Hamsters. *Viruses* **2020**, *12*, doi:10.3390/v12070779.
35. Halfmann, P.J.; Hatta, M.; Chiba, S.; Maemura, T.; Fan, S.; Takeda, M.; Kinoshita, N.; Hattori, S.I.; Sakai-Tagawa, Y.; Iwatsuki-Horimoto, K., et al. Transmission of SARS-CoV-2 in Domestic Cats. *N Engl J Med* **2020**, *383*, 592-594, doi:10.1056/NEJMc2013400.
36. Freuling, C.M.; Breithaupt, A.; Müller, T.; Sehl, J.; Balkema-Buschmann, A.; Rissmann, M.; Klein, A.; Wylezich, C.; Höper, D.; Wernike, K., et al. Susceptibility of raccoon dogs for experimental SARS-CoV-2 infection. *bioRxiv* **2020**, 10.1101/2020.08.19.256800, doi:10.1101/2020.08.19.256800.
37. Mykytyn, A.Z.; Lamers, M.M.; Okba, N.M.A.; Breugem, T.I.; Schipper, D.; van den Doel, P.B.; van Run, P.; van Amerongen, G.; Waal, L.d.; Koopmans, M.P.G., et al. Susceptibility of rabbits to SARS-CoV-2. *bioRxiv* **2020**, 10.1101/2020.08.27.263988, doi:10.1101/2020.08.27.263988.
38. Bao, L.; Deng, W.; Huang, B.; Gao, H.; Liu, J.; Ren, L.; Wei, Q.; Yu, P.; Xu, Y.; Qi, F., et al. The pathogenicity of SARS-CoV-2 in hACE2 transgenic mice. *Nature* **2020**, *583*, 830-833, doi:10.1038/s41586-020-2312-y.
39. Sun, S.H.; Chen, Q.; Gu, H.J.; Yang, G.; Wang, Y.X.; Huang, X.Y.; Liu, S.S.; Zhang, N.N.; Li, X.F.; Xiong, R., et al. A Mouse Model of SARS-CoV-2 Infection and Pathogenesis. *Cell Host Microbe* **2020**, *28*, 124-133 e124, doi:10.1016/j.chom.2020.05.020.
40. Winkler, E.S.; Bailey, A.L.; Kafai, N.M.; Nair, S.; McCune, B.T.; Yu, J.; Fox, J.M.; Chen, R.E.; Earnest, J.T.; Keeler, S.P., et al. SARS-CoV-2 infection of human ACE2-transgenic mice causes severe lung inflammation and impaired function. *Nat Immunol* **2020**, 10.1038/s41590-020-0778-2, doi:10.1038/s41590-020-0778-2.
41. Ulrich, L.; Wernike, K.; Hoffmann, D.; Mettenleiter, T.C.; Beer, M. Experimental Infection of Cattle with SARS-CoV-2. *Emerg Infect Dis* **2020**, *26*, doi:10.3201/eid2612.203799.
42. Munster, V.J.; Feldmann, F.; Williamson, B.N.; van Doremalen, N.; Perez-Perez, L.; Schulz, J.; Meade-White, K.; Okumura, A.; Callison, J.; Brumbaugh,

B., et al. Respiratory disease in rhesus macaques inoculated with SARS-CoV-2. *Nature* **2020**, *585*, 268-272, doi:10.1038/s41586-020-2324-7.

43. Shan, C.; Yao, Y.F.; Yang, X.L.; Zhou, Y.W.; Gao, G.; Peng, Y.; Yang, L.; Hu, X.; Xiong, J.; Jiang, R.D., et al. Infection with novel coronavirus (SARS-CoV-2) causes pneumonia in Rhesus macaques. *Cell Res* **2020**, *30*, 670-677, doi:10.1038/s41422-020-0364-z.
44. Lu, S.; Zhao, Y.; Yu, W.; Yang, Y.; Gao, J.; Wang, J.; Kuang, D.; Yang, M.; Yang, J.; Ma, C., et al. Comparison of nonhuman primates identified the suitable model for COVID-19. *Signal Transduct Target Ther* **2020**, *5*, 157, doi:10.1038/s41392-020-00269-6.
45. Suarez, D.L.; Pantin-Jackwood, M.J.; Swayne, D.E.; Lee, S.A.; DeBlois, S.M.; Spackman, E. Lack of susceptibility of poultry to SARS-CoV-2 and MERS-CoV. *bioRxiv* **2020**, 10.1101/2020.06.16.154658, doi:10.1101/2020.06.16.154658.
46. Martines, R.B.; Ritter, J.M.; Matkovic, E.; Gary, J.; Bollweg, B.C.; Bullock, H.; Goldsmith, C.S.; Silva-Flannery, L.; Seixas, J.N.; Reagan-Steiner, S., et al. Pathology and Pathogenesis of SARS-CoV-2 Associated with Fatal Coronavirus Disease, United States. *Emerg Infect Dis* **2020**, *26*, 2005-2015, doi:10.3201/eid2609.202095.
47. Schaefer, I.M.; Padera, R.F.; Solomon, I.H.; Kanjilal, S.; Hammer, M.M.; Hornick, J.L.; Sholl, L.M. In situ detection of SARS-CoV-2 in lungs and airways of patients with COVID-19. *Mod Pathol* **2020**, 10.1038/s41379-020-0595-z, doi:10.1038/s41379-020-0595-z.
48. Matryba, P.; Kaczmarek, L.; Golab, J. Advances in Ex Situ Tissue Optical Clearing. *Laser & Photonics Reviews* **2019**, *13*, doi:10.1002/lpor.201800292.
49. Potratz, M.; Zaeck, L.; Christen, M.; Te Kamp, V.; Klein, A.; Nolden, T.; Freuling, C.M.; Muller, T.; Finke, S. Astrocyte Infection during Rabies Encephalitis Depends on the Virus Strain and Infection Route as Demonstrated by Novel Quantitative 3D Analysis of Cell Tropism. *Cells* **2020**, *9*, doi:10.3390/cells9020412.
50. Zaeck, L.; Potratz, M.; Freuling, C.M.; Muller, T.; Finke, S. High-Resolution 3D Imaging of Rabies Virus Infection in Solvent-Cleared Brain Tissue. *J Vis Exp* **2019**, 10.3791/59402, doi:10.3791/59402.
51. Kieffer, C.; Ladinsky, M.S.; Ninh, A.; Galimidi, R.P.; Bjorkman, P.J. Longitudinal imaging of HIV-1 spread in humanized mice with parallel 3D immunofluorescence and electron tomography. *Elife* **2017**, *6*, doi:10.7554/eLife.23282.
52. Potratz, M.; Zaeck, L.M.; Weigel, C.; Klein, A.; Freuling, C.M.; Müller, T.; Finke, S. Neuroglia Infection by Rabies Virus after Anterograde Virus Spread in Peripheral Neurons. *bioRxiv* **2020**, 10.1101/2020.09.20.305078, doi:10.1101/2020.09.20.305078.
53. Ladinsky, M.S.; Khamaikawin, W.; Jung, Y.; Lin, S.; Lam, J.; An, D.S.; Bjorkman, P.J.; Kieffer, C. Mechanisms of virus dissemination in bone marrow of HIV-1-infected humanized BLT mice. *Elife* **2019**, *8*, doi:10.7554/eLife.46916.
54. Chhatbar, C.; Detje, C.N.; Grabski, E.; Borst, K.; Spanier, J.; Ghita, L.; Elliott, D.A.; Jordao, M.J.C.; Mueller, N.; Sutton, J., et al. Type I Interferon Receptor Signaling of Neurons and Astrocytes Regulates Microglia Activation during Viral Encephalitis. *Cell Rep* **2018**, *25*, 118-129 e114, doi:10.1016/j.celrep.2018.09.003.

55. Eckermann, M.; Frohn, J.; Reichardt, M.; Osterhoff, M.; Sprung, M.; Westermeier, F.; Tzankov, A.; Werlein, C.; Kuhnel, M.; Jonigk, D., et al. 3D virtual pathohistology of lung tissue from Covid-19 patients based on phase contrast X-ray tomography. *Elife* **2020**, *9*, doi:10.7554/eLife.60408.
56. Li, G.; Fox, S.E.; Summa, B.; Hu, B.; Wenk, C.; Akmatbekov, A.; Harbert, J.L.; Vander Heide, R.S.; Brown, J.Q. Multiscale 3-dimensional pathology findings of COVID-19 diseased lung using high-resolution cleared tissue microscopy. *bioRxiv* **2020**, 10.1101/2020.04.11.037473, doi:10.1101/2020.04.11.037473.
57. Bussmann, B.M.; Reiche, S.; Jacob, L.H.; Braun, J.M.; Jassoy, C. Antigenic and cellular localisation analysis of the severe acute respiratory syndrome coronavirus nucleocapsid protein using monoclonal antibodies. *Virus Res* **2006**, *122*, 119-126, doi:10.1016/j.virusres.2006.07.005.
58. Renier, N.; Wu, Z.; Simon, D.J.; Yang, J.; Ariel, P.; Tessier-Lavigne, M. iDISCO: a simple, rapid method to immunolabel large tissue samples for volume imaging. *Cell* **2014**, *159*, 896-910, doi:10.1016/j.cell.2014.10.010.
59. Klingberg, A.; Hasenberg, A.; Ludwig-Portugall, I.; Medyukhina, A.; Mann, L.; Brenzel, A.; Engel, D.R.; Figge, M.T.; Kurts, C.; Gunzer, M. Fully Automated Evaluation of Total Glomerular Number and Capillary Tuft Size in Nephritic Kidneys Using Lightsheet Microscopy. *Journal of the American Society of Nephrology : JASN* **2017**, *28*, 452-459, doi:10.1681/ASN.2016020232.
60. Amich, J.; Mokhtari, Z.; Strobel, M.; Vialetto, E.; Sheta, D.; Yu, Y.; Hartweg, J.; Kalleda, N.; Jarick, K.J.; Brede, C., et al. Three-Dimensional Light Sheet Fluorescence Microscopy of Lungs To Dissect Local Host Immune-Aspergillus fumigatus Interactions. *mBio* **2020**, *11*, doi:10.1128/mBio.02752-19.
61. Pichat, J.; Iglesias, J.E.; Yousry, T.; Ourselin, S.; Modat, M. A Survey of Methods for 3D Histology Reconstruction. *Med Image Anal* **2018**, *46*, 73-105, doi:10.1016/j.media.2018.02.004.
62. Merz, S.F.; Jansen, P.; Ulankiewicz, R.; Bornemann, L.; Schimming, T.; Griewank, K.; Cibir, Z.; Kraus, A.; Stoffels, I.; Aspelmeier, T., et al. High-resolution 3-D imaging for precise staging in malignant melanoma. *medRxiv* **2020**, 10.1101/2020.07.22.20159103, doi:10.1101/2020.07.22.20159103.
63. Enkirch, T.; von Messling, V. Ferret models of viral pathogenesis. *Virology* **2015**, *479-480*, 259-270, doi:10.1016/j.virol.2015.03.017.
64. Puelles, V.G.; Lutgehetmann, M.; Lindenmeyer, M.T.; Sperhake, J.P.; Wong, M.N.; Allweiss, L.; Chilla, S.; Heinemann, A.; Wanner, N.; Liu, S., et al. Multiorgan and Renal Tropism of SARS-CoV-2. *N Engl J Med* **2020**, *383*, 590-592, doi:10.1056/NEJMc2011400.
65. Ramani, A.; Muller, L.; Ostermann, P.N.; Gabriel, E.; Abida-Islam, P.; Muller-Schiffmann, A.; Mariappan, A.; Goureau, O.; Gruell, H.; Walker, A., et al. SARS-CoV-2 targets neurons of 3D human brain organoids. *EMBO J* **2020**, *39*, e106230, doi:10.15252/embj.2020106230.

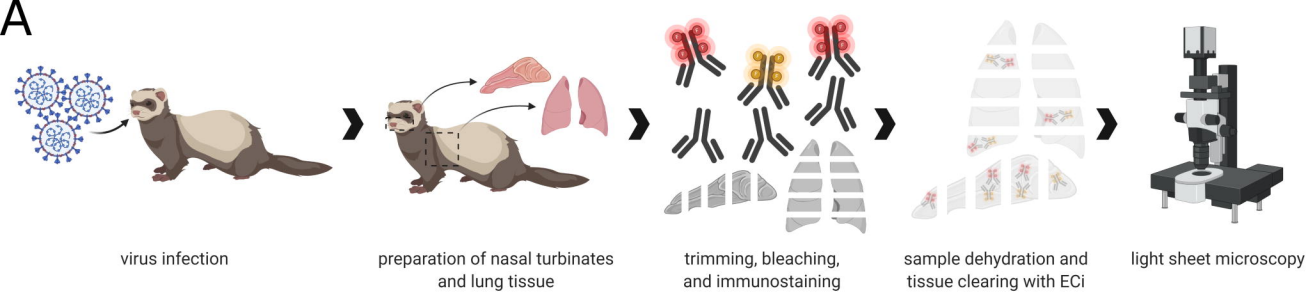

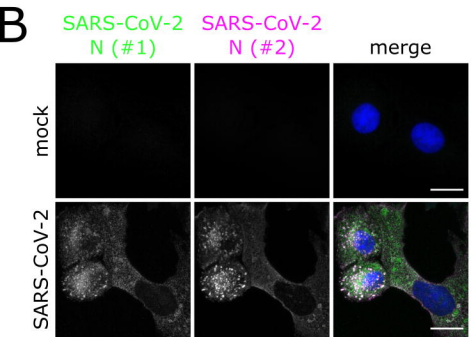

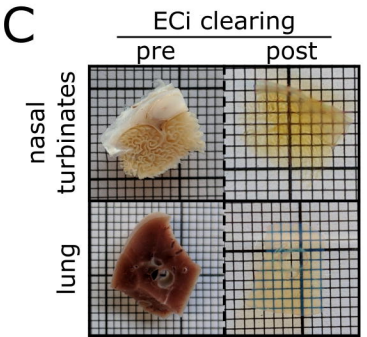

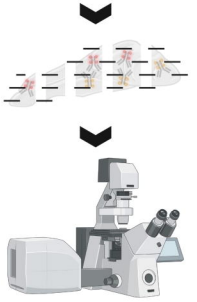

slicing of cleared samples to 1 mm thickness

confocal laser scanning microscopy

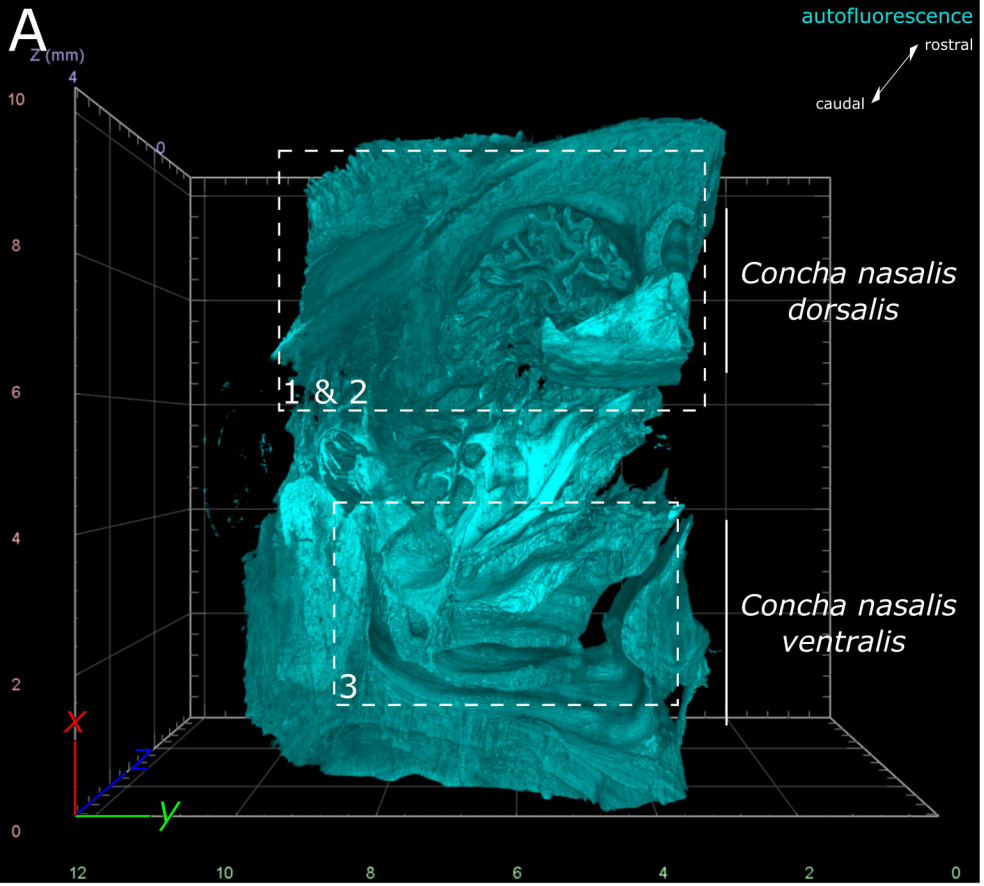
A
autofluorescence
rostral
caudal
Z (mm)
Concha nasalis dorsalis
Concha nasalis ventralis
1 & 2
3
X
Z
y

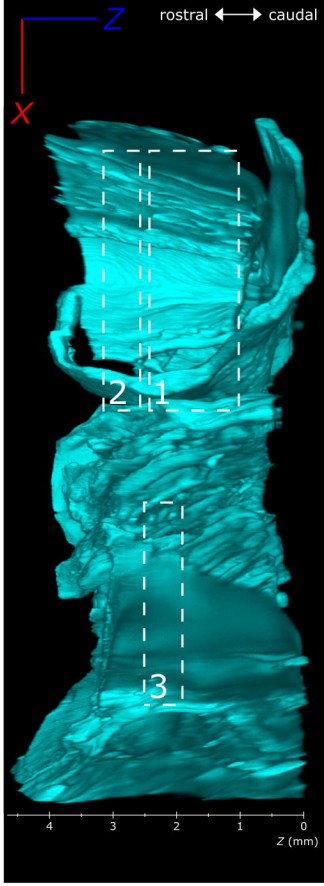
Z
rostral
caudal
X
2
1
3
Z (mm)

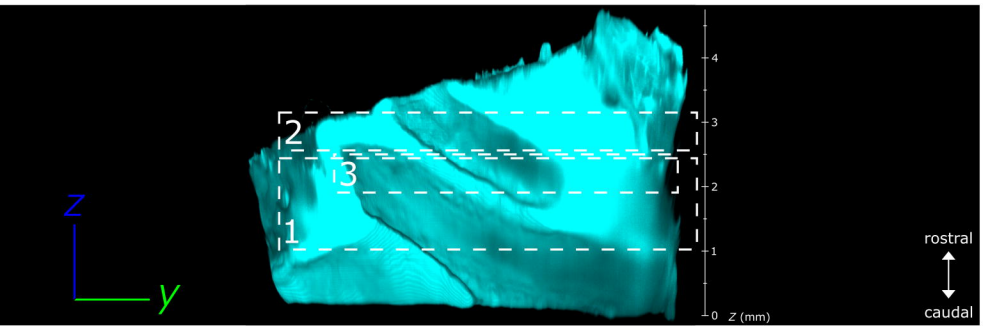
2
3
1
Z
y
rostral
caudal
Z (mm)

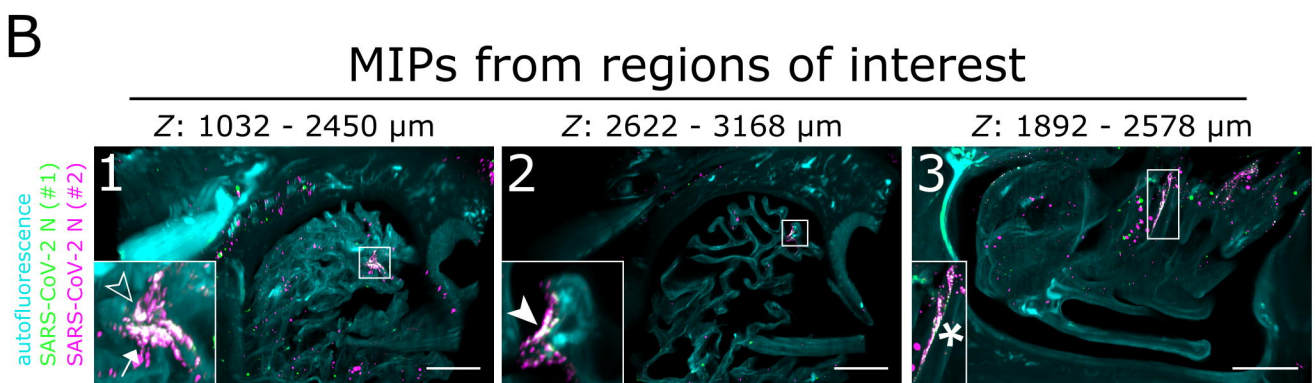
B
MIPs from regions of interest
Z: 1032 - 2450 µm
Z: 2622 - 3168 µm
Z: 1892 - 2578 µm
autofluorescence
SARS-CoV-2 N (#1)
SARS-CoV-2 N (#2)
1
2
3

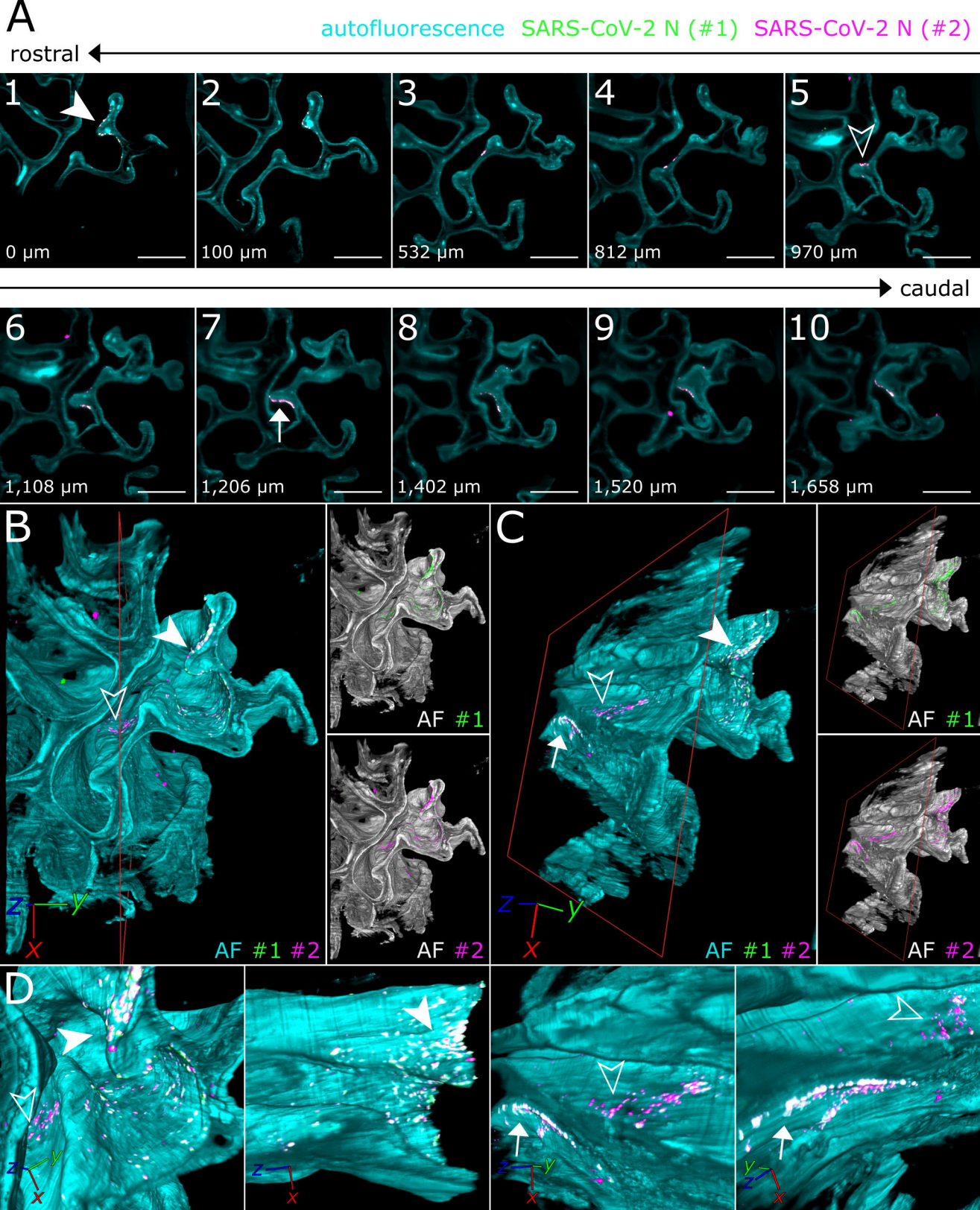
A
autofluorescence
SARS-CoV-2 N (#1)
SARS-CoV-2 N (#2)
rostral
caudal
1
2
3
4
5
0 µm
100 µm
532 µm
812 µm
970 µm
6
7
8
9
10
1,108 µm
1,206 µm
1,402 µm
1,520 µm
1,658 µm
B
AF #1
AF #2
AF #1 #2
C
AF #1
AF #2
AF #1 #2
D

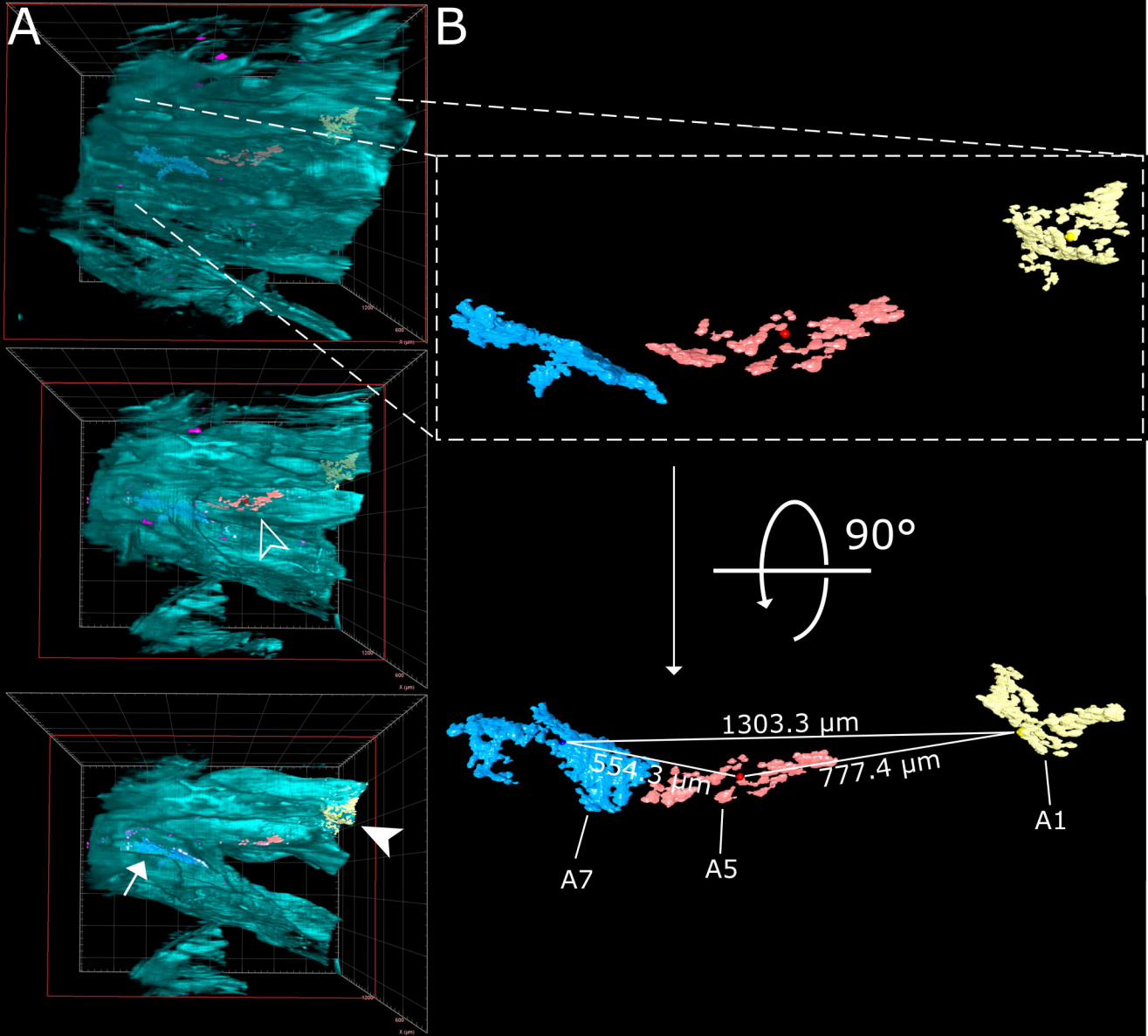
A
B
90°
1303.3 µm
554.3 µm
777.4 µm
A7
A5
A1

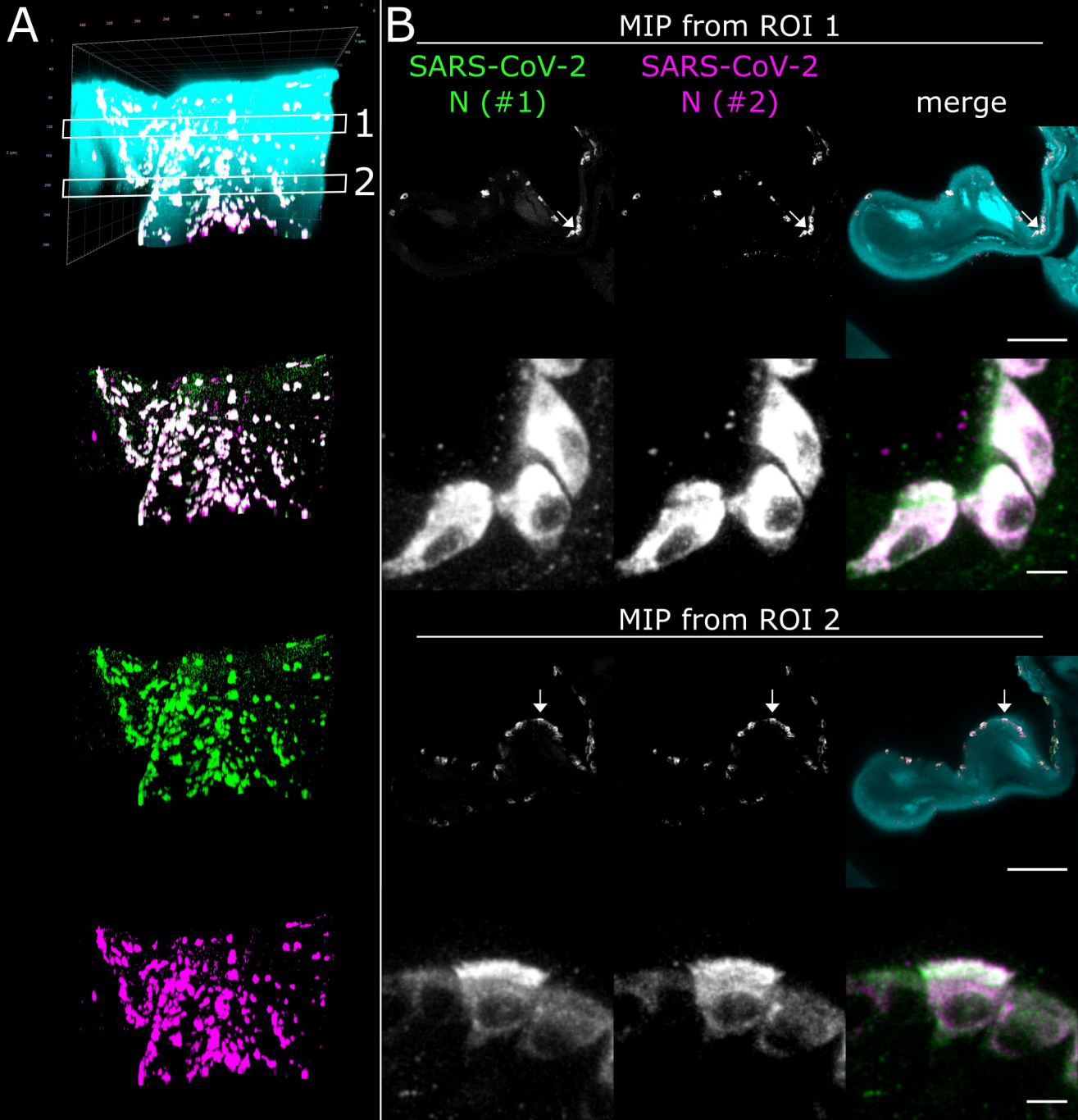
A
1
2
B
MIP from ROI 1
SARS-CoV-2
N (#1)
SARS-CoV-2
N (#2)
merge
MIP from ROI 2

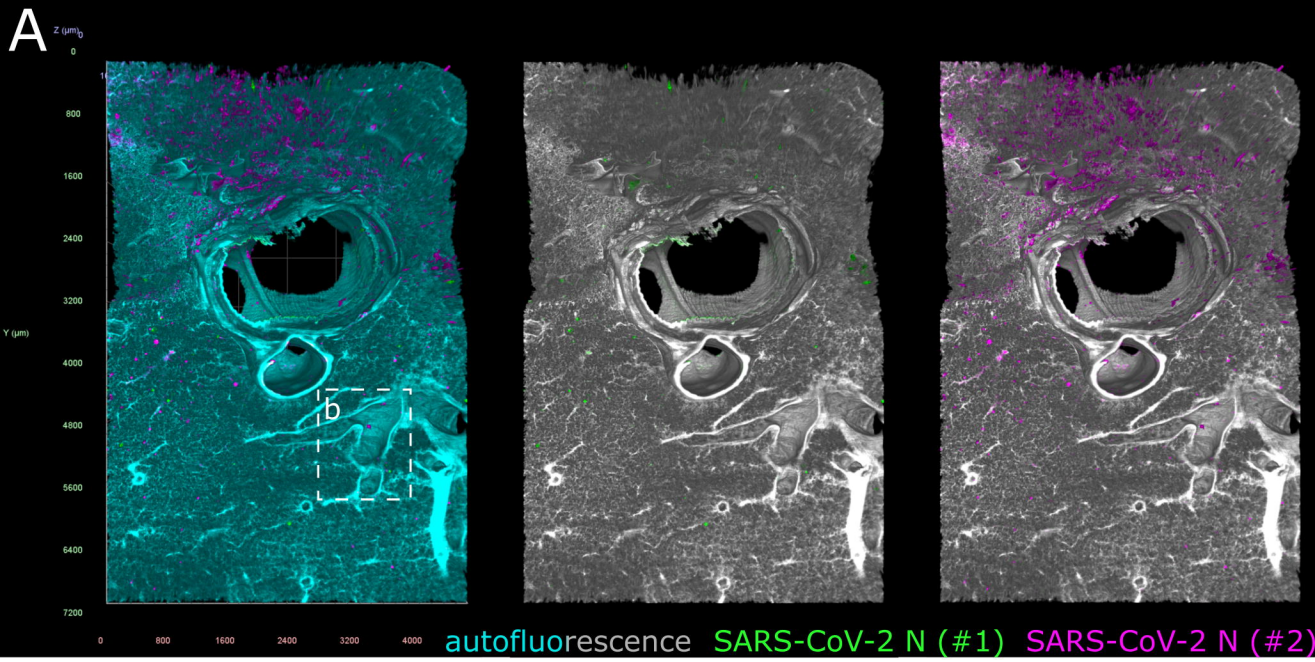
A
Z (µm)
0
800
1600
2400
3200
Y (µm)
4000
4800
5600
6400
7200
b
0
800
1600
2400
3200
4000
autofluorescence
SARS-CoV-2 N (#1)
SARS-CoV-2 N (#2)

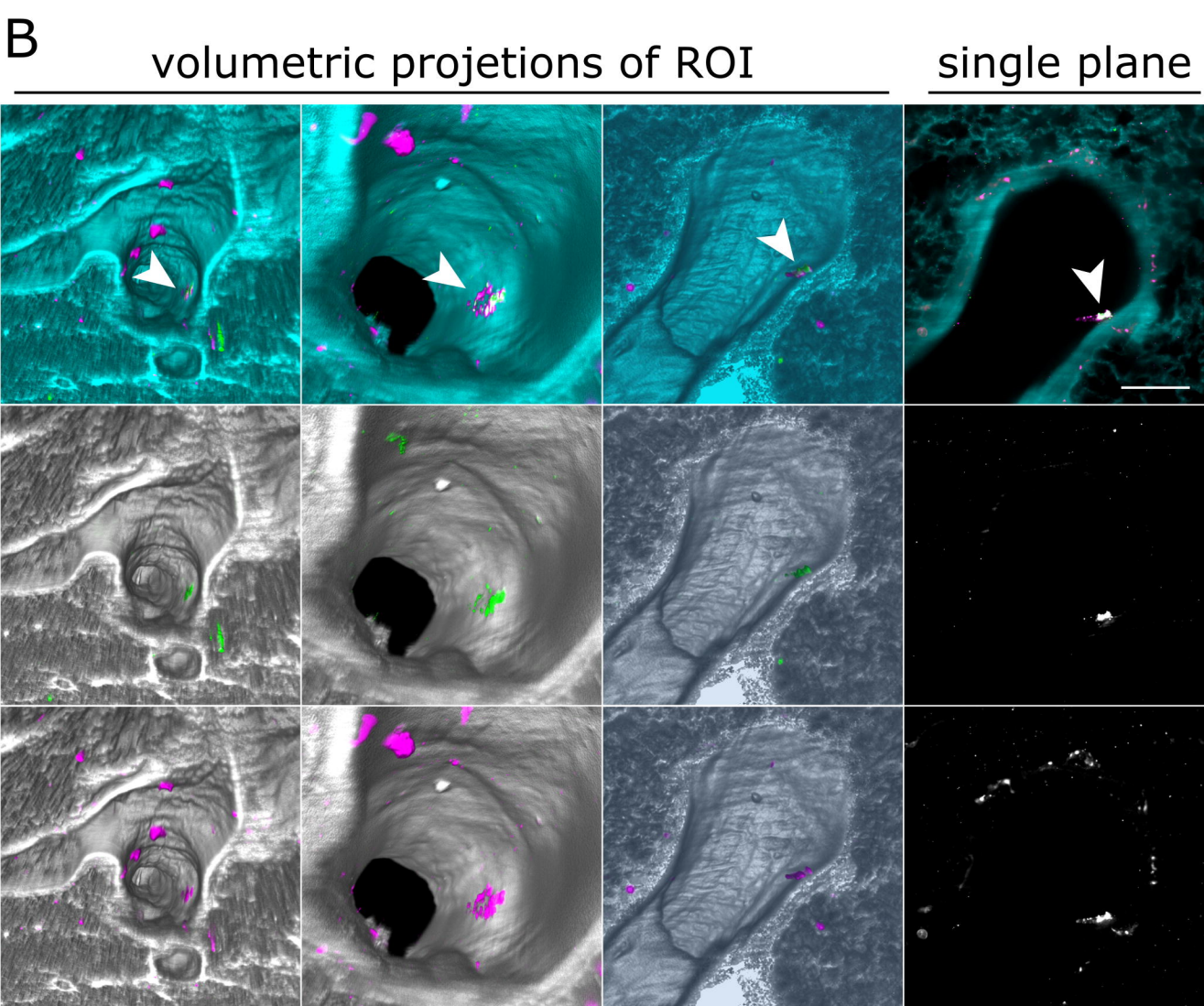
B
volumetric projetions of ROI
single plane